



Deltoidal icositetrahedron faceting on α -Fe crystals found on the surface of the Moon

Kevin M. Knowles^{a,*}, Harshad K.D.H. Bhadeshia^{a,b}

^a Department of Materials Science and Metallurgy, University of Cambridge, 27 Charles Babbage Road, Cambridge CB3 0FS, UK

^b School of Engineering and Materials Science, Queen Mary University of London, Mile End Road, London E1 4NS, UK

ARTICLE INFO

Communicated by: Alexander Van Driessche

Keywords:

A1 Crystallography
A1 Crystal morphology
A1 Scanning electron microscopy
A2 Growth from vapor
A2 Single crystal growth
B1 Iron

ABSTRACT

Crystallographic analysis of scanning electron microscopy images of small μm -sized single crystals of b.c.c. iron found on the surface of the Moon shows that the deltoidal icositetrahedron faceting behaviour clearly seen is best describable as being from planes of the $\{229\}$ form. While possibly unexpected given the lack of any report of such faceting in terrestrial and meteoritic b.c.c. iron single crystals, this deltoidal icositetrahedron faceting behaviour can be rationalised straightforwardly in terms of the local chemical conditions which will have been experienced by these crystals while growing from the vapour in the part of the lunar environment from which these samples were obtained.

1. Introduction

Some fifty years ago, Clanton et al. [1–4] reported scanning electron microscope observations of b.c.c. iron crystals found as small μm -sized single crystals in lunar samples from the various Apollo missions to the Moon. Energy dispersive X-ray analysis of these b.c.c. iron crystals showed that levels of nickel, phosphorus, cobalt and sulfur were below the detection limit of the instrumentation, reported as 0.5% [1–4], indicating that they were therefore of high purity. Interestingly, Clanton et al. reported that these b.c.c. iron crystals exhibited six of the seven possible forms of the holosymmetric class $m\bar{3}m$ [3–5]. In contrast to these observations, observations of iron crystals produced as single crystals on Earth have a more restricted range of morphologies. From surface energy considerations, and also from experimental observations, the morphology of such crystals is expected to be dominated by $\{110\}$ and $\{100\}$ planes (or facets) [6,7]. In addition to these planes bounding b.c.c. iron crystals, large $\{111\}$ facets and small $\{112\}$ facets have also been reported recently on plastically deformed and carefully annealed b.c.c. iron nanocrystals [8].

An example of a small group of iron crystals found in a small cavity of recrystallised fragmented rock from the Apollo 15 Hadley-Apennine lunar landing site is shown in Fig. 1 [9]. The largest crystal here is reported to be three micrometres across. These three crystals would all seem to have the same facet morphology. They are seen to be formed of

$\{100\}$ cube planes and $\{hhl\}$ planes of a deltoidal icositetrahedron form with $l > h$ so that for each crystal the overall shape is describable as a truncated deltoidal icositetrahedron. As a consequence of the presence of the $\{100\}$ planes, the $\{hhl\}$ planes each have five edges. Fig. 2 of [1] and also Fig. 2 of [2] where Clanton et al. refer to the $\{hhl\}$ form as the trapezohedron form are both part of the image shown here in Fig. 1. The trapezohedron nomenclature used by Clanton et al. [1,2] is equivalent to describing this form as the deltoidal icositetrahedron form, as we have chosen to do here, or, alternatively, simply the icositetrahedron form, the nomenclature favoured by Phillips [5].

Interestingly, there is no further crystallographic analysis in the literature of the $\{hhl\}$ form seen in Fig. 1, or indeed the $\{hhl\}$ forms in Figs. 2 and 3, reproduced from the two Clanton et al. papers [2,4], respectively. The figure captions accompanying these latter figures in these two papers suggest that for both crystals there are two separate sets of $\{hhl\}$ forms. While there is clear evidence for this surrounding one of the $\langle 111 \rangle$ directions of the iron crystal in Fig. 3, the evidence for two separate sets of $\{hhl\}$ forms in Fig. 2 here would seem to have been lost in the process of reproduction into the journal image from the original scanning electron microscope image. Even though Fig. 2 is taken from a 45 MB high resolution scan of a printed version of the Clanton et al. paper, this printed version had already lost subtleties in contrast presumed to be apparent in the original image. It is evident from Fig. 3 here that the contrast between the two different sets of $\{hhl\}$ forms is indeed

* Corresponding author.

E-mail address: kmk10@cam.ac.uk (K.M. Knowles).

<https://doi.org/10.1016/j.jcrysgro.2023.127257>

Received 17 February 2023; Received in revised form 4 May 2023; Accepted 9 May 2023

Available online 13 May 2023

0022-0248/© 2023 The Author(s). Published by Elsevier B.V. This is an open access article under the CC BY license (<http://creativecommons.org/licenses/by/4.0/>).

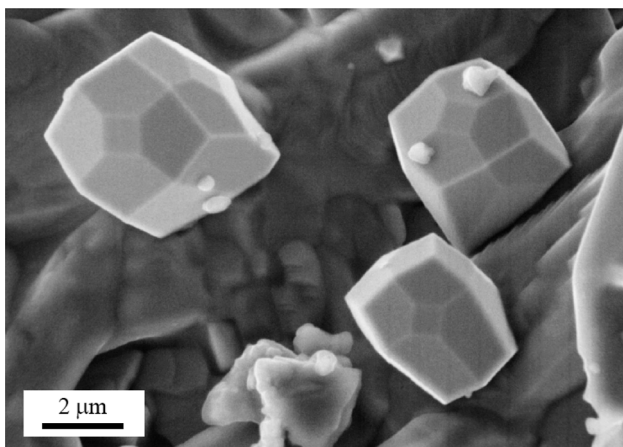


Fig. 1. Part of NASA image S72-55208 from the Apollo 15 mission to the Moon. Three iron crystals with $\{100\}$ faceting and $\{hhl\}$ deltooidal icositetrahedral faceting are evident in this scanning electron microscope image.

subtle, implying that the angular difference between these two sets is clearly a few degrees at most.

The problem of determining suitable h and l for the five crystals in Fig. 1 and the further two in Figs. 2 and 3 is a projectional geometry problem where the unknown direction $[uvw]$ along which the crystals are projected, and the precise details of the unknown faces of the form $\{hhl\}$ for suitable h and l , with $l > h$ need to be determined. This is a classical crystallography problem which makes use of the concept of the law of constancy of angle, and it requires an understanding of the way in which a two-dimensional image in a scanning electron microscope relates to the three-dimensional shape being imaged. It is the purpose of this paper to solve this problem for the deltooidal icositetrahedra $\{hhl\}$ forms seen in Figs. 1-3 and to comment on the nature of these forms in the wider context of the growth of α -Fe single crystals.

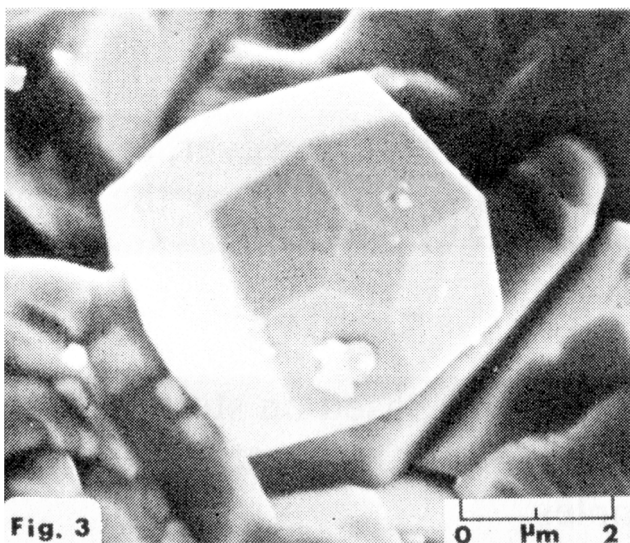


Fig. 2. Fig. 3 from Clanton et al. [2]. The authors assert that there are two sets of $\{hhl\}$ faceting evident on this scanning electron microscope image of an iron crystal, with a smaller set of $\{100\}$ faceting. However, although this image is taken from a high-resolution scan of a printed version of the Clanton et al. paper, the two sets of $\{hhl\}$ faceting are not evident. Instead, only one $\{100\}$ facet together with its four nearest neighbours of one set of $\{hhl\}$ facets are readily visible.

2. Crystallographic analysis

The μm -sized dimensions of the five iron crystals in Figs. 1-3 is such that it is entirely reasonable to make the assumption that the projective geometry here is that of parallel projection, so that the centre of projection is at infinity. This approximation is suggested by Cornille [10] as being suitable for magnifications in the scanning electron microscope above 20,000; it is still likely to be a reasonable approximation for the unknown actual magnifications of the original NASA images from which Figs. 1-3 here were taken. Hence, with this assumption, the projectional geometry seen at this magnification in a scanning electron microscope is that of an orthographic projection of each crystal. It follows that the facets of the crystals seen in Figs. 1-3 are seen as though they are projected onto the plane normal to a direction $[uvw]$ in the coordinates of the b.c.c. unit cell of iron defining the projection direction for each crystal.

Inspection of each of the five iron crystals in Figs. 1-3 shows that furthermore it is reasonable to assume that the cube $\{100\}$ planes are squares for all five crystals, even though it is evident that for the upper right crystal in Fig. 1 and the crystal in Fig. 3 that the $\{100\}$ planes do not all have the same size. For the crystal in the lower right of Fig. 1, it is apparent that two of the four $\{hhl\}$ planes surrounding the top $\{100\}$ plane have clearly been elongated along one of their directions, whereas the other two do not seem elongated. Hence, for the purposes of analysis, the different crystals have been taken to be of the three external morphologies described in Sections 2.1-2.3:

2.1. The crystal in the upper left of Fig. 1 and the crystal in Fig. 2

For these two crystals, their external forms have been taken to be ones with $m\bar{3}m$ symmetry, so that each $\{100\}$ plane is of the same size and shape, and each plane of the $\{hhl\}$ form, i.e., each $\{hhl\}$ facet, is of the same size and shape. For the specific facet labelled (hhl) for $l > h$, the neighbouring faces are (001) , $(\bar{h}hl)$, (hlh) , (lhh) and $(h\bar{h}l)$, so that the five vectors defining the borders of (hhl) are $\pm[1\bar{1}0]$, $\pm[0\bar{l}h]$, $\pm[l^2-h^2, h^2-hl, h^2-hl]$, $\pm[h^2-hl, l^2-h^2, h^2-hl]$ and $\pm[l0\bar{h}]$, respectively.

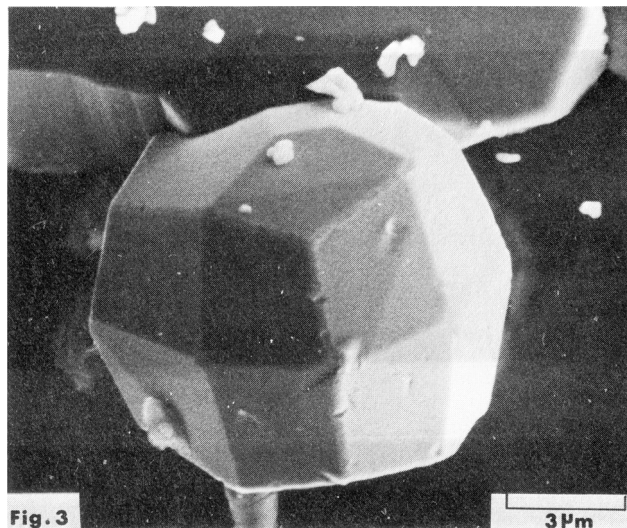


Fig. 3. Fig. 3 from Clanton et al. [4]. This is also a scanning electron micrograph. It is evident that there are two sets of $\{hhl\}$ faceting surrounding one of the $\langle 111 \rangle$ directions of this iron crystal. In addition, there is a much smaller set of $\{100\}$ faceting. The subtlety in contrast between the two sets of $\{hhl\}$ faceting is such that the angular difference between these two sets is clearly a few degrees at most.

It is convenient to let the line common to (hhl) and (001) be of unit length. We can then choose the length of the lines common to (i) (hhl) and $(\bar{h}hl)$ and (ii) (hhl) and $(h\bar{h}l)$ to be α times in length that of the line common to (hhl) and (001) .

Likewise, the lines common to (i) (hhl) and (hlh) , and (ii) (hhl) and (lhh) will both be β times in length that of the line common to (hhl) and (001) .

Starting from the centre of the (001) face, we therefore have the identity

$$\begin{aligned} & \left[0, \frac{1}{\sqrt{2}}, 0\right] + \frac{\alpha}{\sqrt{h^2 + l^2}} [0, l, -h] + \frac{\beta}{\Pi} [l^2 - h^2, h^2 - hl, h^2 - hl] + \\ & - \frac{\beta}{\Pi} [h^2 - hl, l^2 - h^2, h^2 - hl] + \frac{\alpha}{\sqrt{h^2 + l^2}} [-l, 0, h] + \left[-\frac{1}{\sqrt{2}}, 0, 0\right] \equiv 0 \end{aligned} \tag{1}$$

to determine β given α , where $\Pi^2 = (l^2 - h^2)^2 + 2(h^2 - hl)^2 = l^4 + 3h^4 - 4h^3l$. Hence, equating either the x - or the y -coefficients in this equation, it is evident that

$$\beta = \frac{\Pi}{(l^2 + hl - 2h^2)} \left(\frac{1}{\sqrt{2}} + \frac{\alpha l}{\sqrt{h^2 + l^2}} \right) \tag{2}$$

Suppose now that the origin is shifted to the centre of this crystal with external $m\bar{3}m$ symmetry, so that the vector to the (001) face from the origin is of the form $[0, 0, n]$ for some n . The vector $[0, n, 0]$ then specifies the centre of the (010) face. Starting from the centre of the cube, we therefore have the identity

$$\begin{aligned} & [0, 0, n] + \left[0, \frac{1}{\sqrt{2}}, 0\right] + \frac{\alpha}{\sqrt{h^2 + l^2}} [0, l, -h] + \frac{\alpha}{\sqrt{h^2 + l^2}} [0, h, -l] + [0, 0, -\frac{1}{\sqrt{2}}] \\ & + [0, -n, 0] \equiv 0 \end{aligned} \tag{3}$$

Hence, equating either the y - or the z -coefficients in this equation, it is evident that

$$n = \frac{1}{\sqrt{2}} + \frac{\alpha(h+l)}{\sqrt{h^2 + l^2}} \tag{4}$$

These calculations help to determine how such a crystal with $\{001\}$ and $\{hhl\}$ interfaces and external $m\bar{3}m$ symmetry is seen in an orthographic projection along various possible $[uvw]$ projection directions.

Another useful result is that the projection direction $[uvw]$ for such a crystal with exact external $m\bar{3}m$ symmetry can be deduced from the external shape of the crystal seen in projection: the projection direction will be at the point where lines linking opposite vertices of the perimeter of this external shape all meet. A close inspection of both the crystal in the upper left of Fig. 1 and the crystal in Fig. 2 shows that this useful result is able to establish narrow bounds both for the projection directions $[uvw]$ of these two crystals and suitable $\{hhl\}$ forms for the deltoidal icositetrahedron faceting behaviour.

2.2. The crystal in the upper right of Fig. 1 and the crystal in Fig. 3

For these two crystals, the assumption for modelling purposes is that the $\{hhl\}$ facets would all be identical in the absence of the planes of the $\{100\}$ form. Therefore, for an (001) plane as a ‘reference’ facet where the line common to (hhl) and (001) is of unit length, we can let a clearly larger (010) or (100) facet have facet sides of length γ_1 . To compensate for this, it is evident that for this larger facet, α must decrease to a value α_1 , defined by the identity

$$\frac{\gamma_1}{\sqrt{2}} + \frac{\alpha_1 l}{\sqrt{h^2 + l^2}} = \frac{1}{\sqrt{2}} + \frac{\alpha l}{\sqrt{h^2 + l^2}} \tag{5}$$

since the terms in β in Eq. (1) are unchanged by the assumption that the $\{hhl\}$ facets would all be identical in shape in the absence of the $\{100\}$ facets. This therefore is a minor adjustment to the two crystals whose

external morphology can be taken to have external $m\bar{3}m$ symmetry.

Furthermore, just like the two crystals which can be taken to be ones with exact external $m\bar{3}m$ symmetry, as long as the lines joining opposite vertices of the external shape are chosen with care, narrow bounds both for the projection directions $[uvw]$ of these two crystals and suitable $\{hhl\}$ for the deltoidal icositetrahedron faceting can usefully be determined.

2.3. The crystal in the lower right of Fig. 1

For this crystal, it is evident that the shape of the crystal is far from the ideal external $m\bar{3}m$ symmetry, and so we have to generalise equation (1) for facets of a more general shape, while keeping the line common to (hhl) and (001) to be of unit length. Suppose the (hhl) face is one of these elongated faces clearly seen on this crystal in Fig. 1. It has the vector $[0l\bar{h}]$ of magnitude α_1 relative to $\pm [1\bar{1}0]$ vector of unit length, and it has the vector $[\bar{l}0h]$ of magnitude α_2 relative to the $\pm [1\bar{1}0]$ vector of unit length. A more general form of equation (1) then becomes

$$\begin{aligned} & \left[0, \frac{1}{\sqrt{2}}, 0\right] + \frac{\alpha_1}{\sqrt{h^2 + l^2}} [0, l, -h] + \frac{\beta_2}{\Pi} [l^2 - h^2, h^2 - hl, h^2 - hl] + \\ & - \frac{\beta_1}{\Pi} [h^2 - hl, l^2 - h^2, h^2 - hl] + \frac{\alpha_2}{\sqrt{h^2 + l^2}} [-l, 0, h] + \left[-\frac{1}{\sqrt{2}}, 0, 0\right] \equiv 0 \end{aligned} \tag{6}$$

for some β_1 and β_2 to be determined. Equating coefficients of the x - and y -coordinates, we then have

$$\frac{\beta_1}{\Pi} (hl - h^2) + \frac{\beta_2}{\Pi} (l^2 - h^2) = \frac{l\alpha_2}{\sqrt{h^2 + l^2}} + \frac{1}{\sqrt{2}} \tag{7}$$

$$\frac{\beta_1}{\Pi} (l^2 - h^2) + \frac{\beta_2}{\Pi} (hl - h^2) = \frac{l\alpha_1}{\sqrt{h^2 + l^2}} + \frac{1}{\sqrt{2}} \tag{8}$$

respectively to solve for β_1 and β_2 . It is evident from these two simultaneous equations that when $\alpha_1 = \alpha_2, \beta_1 = \beta_2$. Expressing equations (9) and (10) in matrix form, we have equations of the form

$$\begin{pmatrix} A_{11} & A_{12} \\ A_{21} & A_{22} \end{pmatrix} \begin{pmatrix} \beta_1 \\ \beta_2 \end{pmatrix} = \begin{pmatrix} C_1 \\ C_2 \end{pmatrix} \tag{9}$$

whence

$$\begin{pmatrix} \beta_1 \\ \beta_2 \end{pmatrix} = \frac{1}{(A_{11}A_{22} - A_{12}A_{21})} \begin{pmatrix} A_{22} & -A_{12} \\ -A_{21} & A_{11} \end{pmatrix} \begin{pmatrix} C_1 \\ C_2 \end{pmatrix} \tag{10}$$

For analysing this crystal, the faces $(\bar{h}hl)$ and $(h\bar{h}l)$ have $\alpha_1 = \alpha_2$, as do the faces on the $(0\bar{1}0)$ side of this truncated deltoidal icositetrahedron, while the faces (hhl) and $(h\bar{h}l)$ have $\alpha_1 \neq \alpha_2$, with $\alpha_2 = 2\alpha_1$.

The (100) ‘face’ of this truncated deltoidal icositetrahedron composed of the five facets $(100), (lhh), (lh\bar{h}), (\bar{l}h\bar{h})$ and (lhh) is not clearly seen in Fig. 1 because it is almost parallel to the electron beam. It must have a different value of α, α_3 , for the length of the four $[\bar{h}l0], [\bar{h}l0], [\bar{h}0l]$ and $[\bar{h}0l]$ vectors on this ‘face’. If the (100) facet on this ‘face’ has sides of unit length, then it is apparent that

$$\alpha_3 = \frac{\sqrt{h^2 + l^2}}{l} \left(\frac{\beta_1}{\Pi} (l^2 + hl - 2h^2) - \frac{1}{\sqrt{2}} \right) \tag{11}$$

In comparison with the other four crystals, it is somewhat more difficult to establish narrow bounds for the projection directions $[uvw]$ of this crystal, but the subtleties of the projectional geometry of the possible $\{hhl\}$ facets for this crystal help in this regard.

2.4. Projectional geometry

For calculations to predict how the five crystals seen in Figs. 1-3 are seen in projection, extensive use was made of the formula for the projected direction, r_p , of a vector r when viewed along a vector $u = [uvw]$ in an orthographic projection of the crystal:

$$r_p = r - \left(\frac{u \cdot r}{u \cdot u} \right) u \quad (12)$$

This formula enabled the directions in projection of the $\{100\}$ and $\{hhl\}$ facet border vectors to be determined, and therefore the lengths of these facet borders also to be determined. Angles seen in projection between different facet borders could also be calculated and compared with the observed values seen in Figs. 1-3. Possible $[uvw]$ projection directions were determined as unit vectors in the form

$$[\cos\phi\sin\theta, \sin\phi\sin\theta, \cos\theta] \quad (13)$$

for different θ and ϕ .

For each crystal, two different approaches were examined to determine the likely families of $\{hhl\}$ facet planes. The first approach was to determine the angles seen in projection between a few prominent facet borders within a crystal and then compare angles determined from the micrographs with those predicted experimentally. This had the advantage of helping to narrow down possible $[uvw]$ projection directions and $\{hhl\}$, but it had the obvious disadvantage of not using all the possible information present in the scanning electron micrographs. Furthermore, for a particular crystal under consideration, it highlighted the need to be able to visualise the entire crystal morphology, and to determine what facets would be visible externally in a particular projection $[uvw]$, and what facets would not be seen. Therefore, a second more systematic and more thorough approach was used. Excel spreadsheets were generated to visualise the entire crystal morphology for each of the five crystals seen in Figs. 1-3 for different $\{hhl\}$ and different $[uvw]$ projection directions consistent with the geometries described in Sections 2.1-2.3. Rotations within the plane (uvw) perpendicular to the plane of projection enabled the predicted crystal morphologies to be oriented conveniently for comparison with the scanning electron micrograph images in Figs. 1-3.

3. Results

Initially, six possible families of likely $\{hhl\}$ facet planes were considered: $\{223\}$, $\{112\}$, $\{113\}$, $\{114\}$, $\{115\}$ and $\{116\}$. However, when comparing different possible projection geometries, subtle differences between possible $\{hhl\}$ facet planes seen in very similar $[uvw]$ projection directions meant that $\{229\}$ facets produced geometries with a better fit to observations for all five crystals in Figs. 1-3 than either $\{114\}$ or $\{115\}$. Since the angular difference between $\{114\}$ and $\{115\}$ is very small – $\cos^{-1}(22/\sqrt{486}) = 3.68^\circ$, $\{229\}$ facet geometries represent a compromise between $\{114\}$ and $\{115\}$. $\{229\}$ is $\cos^{-1}(49/\sqrt{2403}) = 1.65^\circ$ from $\{115\}$ and $\cos^{-1}(40/\sqrt{1602}) = 2.03^\circ$ from $\{114\}$. Given that Clanton et al. saw crystals with two sets of $\{hhl\}$ families, it is entirely reasonable that $\{114\}$ and $\{115\}$ might both be likely candidates for these two sets.

Predicted projectional geometries of each of the five crystals seen in Figs. 1-3 are shown in Figs. 4-8 for all the six $\{hhl\}$ forms considered. The crystal in the top left of Fig. 1 has been used to demonstrate in Fig. 4(b) how the projection direction $[uvw]$ can be deduced from the external shape of this crystal seen in projection, as has been described in Section 2.1.

The $\{229\}$ facet geometry is able to capture the geometry in Fig. 1 slightly better than $\{114\}$ or $\{115\}$ shown in Fig. 4, and noticeably better than $\{116\}$. This can be appreciated by looking at how the $\{hhl\}$ facet clearly visible in the top right-hand corner of the crystal in the top left of Fig. 1 is reproduced for these three forms. It is scarcely visible for the planes of the $\{114\}$ form, visible for planes of the $\{229\}$ and $\{115\}$ forms and arguably less visible in Fig. 1 than would be expected if the planes are of the $\{116\}$ form.

By comparison, the predicted projectional geometries if the facets were $\{223\}$, $\{112\}$ or $\{113\}$ in Fig. 4 are clearly inconsistent with the facet geometry seen in this crystal in Fig. 1. For example, if the $\{hhl\}$

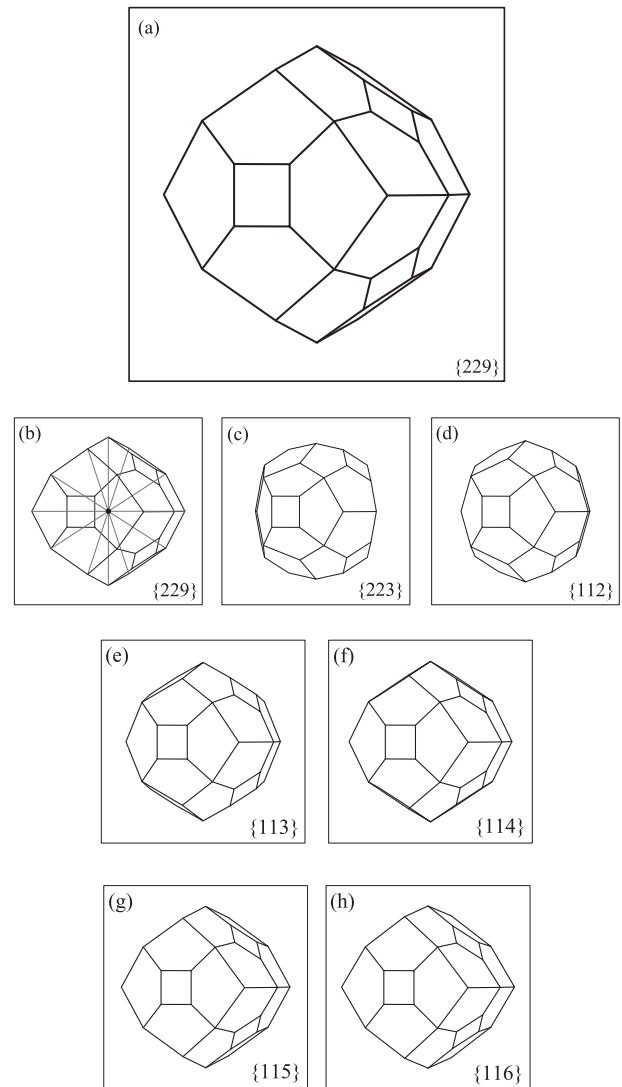


Fig. 4. (a) Reconstruction of the orthographic projectional geometry of the crystal in the top left of Fig. 1, assuming that the $\{hhl\}$ facets are $\{229\}$. The crystal has been taken to have external $m\bar{3}m$ symmetry in terms of its morphology. If the $\{100\}$ facet to the left of the projection is labelled as (001) , that on the lower right is labelled as (100) and that at the upper right is labelled (010) , then the projection direction with $\theta = 27.5^\circ$ and $\phi = 46^\circ$ is $[0.321, 0.332, 0.887]$. (b) As in (a), but with lines in blue linking opposite vertices of the perimeter of the crystal seen in projection. Where these lines meet, shown as a black dot, is the projection direction, drawn from the origin at the centre of this crystal to this position on the surface of the $\{229\}$ facet. (c) – (h) Reconstructions for the projection direction shown in (a) and (b) assuming that the $\{hhl\}$ facets are instead (c) $\{223\}$, (d) $\{112\}$, (e) $\{113\}$, (f) $\{114\}$, (g) $\{115\}$ and (h) $\{116\}$, respectively.

planes were of the form $\{113\}$, the $\{hhl\}$ plane seen in the experimental scanning electron micrograph would not be predicted to be visible from an examination of Fig. 4(e). The difference in appearance between the predicted forms for $\{112\}$ and $\{223\}$ in Fig. 4(d) and (c) respectively and the experimental scanning electron micrograph is accentuated in moving from $\{113\}$ to $\{112\}$ to $\{223\}$.

The difference between the predicted form for $\{115\}$ and $\{229\}$ is very subtle. A close examination of Fig. 4(a) and 4(g) might suggest that in Fig. 4 (a) the external perimeter of the projected crystal in the centre top left part of the crystal is slightly more faithfully reproduced than in Fig. 4(g).

Similar comparisons can be made for the crystal in the top right of Fig. 1, the predictions for which are shown in Fig. 5. Here, it is useful to examine evidence in the predictions for the occurrence in the projections

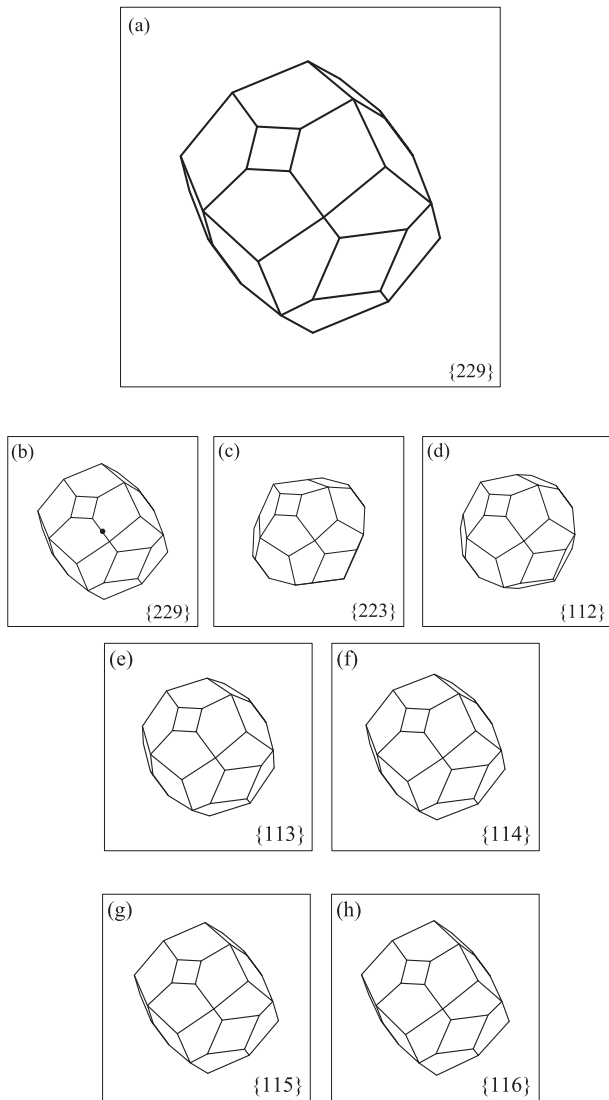


Fig. 5. (a) Reconstruction of the orthographic projectional geometry of the crystal in the top right of Fig. 1, assuming that the $\{hhl\}$ facets are $\{229\}$. The crystal has been taken to have external $m\bar{3}m$ symmetry with respect to the $\{hhl\}$ facets. If the $\{100\}$ facet in the upper left of the projection is labelled as (001) , that on the lower right is labelled as (100) . The (010) and $(0\bar{1}0)$ facets are almost parallel to the projection direction, which with $\theta = 34.5^\circ$ and $\phi = 1^\circ$ is $[0.566, 0.010, 0.824]$. The (100) facet has been made larger than the (001) facet to be consistent with what is seen experimentally in Fig. 1. (b) As in (a), but showing the projection direction, drawn from the origin at the centre of the crystal to the black dot shown on the surface very close to the edge common to the $\{229\}$ and $\{229\}$ facets. (c) – (h) Reconstructions for the projection direction shown in (a) and (b) assuming that the $\{hhl\}$ facets are instead (c) $\{223\}$, (d) $\{112\}$, (e) $\{113\}$, (f) $\{114\}$, (g) $\{115\}$ and (h) $\{116\}$, respectively.

of $(\bar{h}lh)$ and $(\bar{h}\bar{h}h)$ planes; both these planes are present to some very slight degree in the crystal in the top right of Fig. 1. On this basis, it would seem that $\{114\}$, $\{229\}$ and $\{115\}$ provide better predictions than $\{116\}$, and certainly better than $\{113\}$, $\{112\}$ and $\{223\}$. $\{229\}$ is therefore a compromise choice of ‘best fit’.

A comparison of the experimental image of the crystal in the lower right of Fig. 1 with the predictions in Fig. 6 is best made by examining evidence for the relative absence in the predicted images of (lhh) and $(\bar{l}hh)$ facets and the slight hint of presence of $(\bar{h}lh)$ and $(\bar{h}\bar{h}h)$ facets. Here, the predicted images for the $\{114\}$ and $\{115\}$ forms do better than all the others apart from $\{229\}$, but again the differences between $\{114\}$, $\{229\}$ and $\{115\}$ are nuanced.

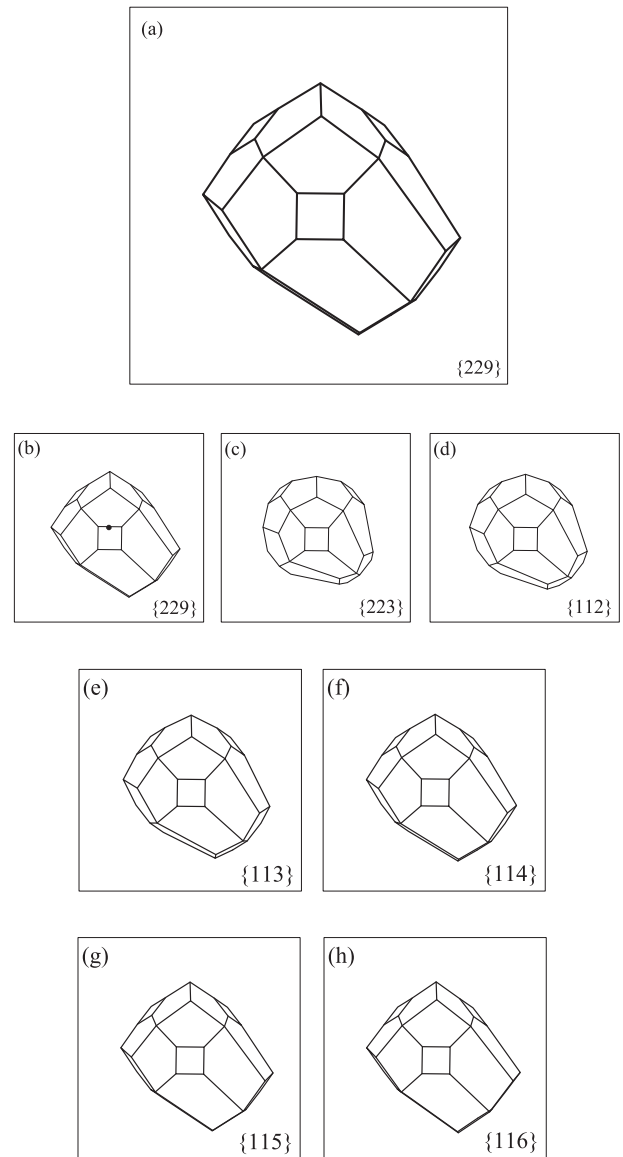


Fig. 6. (a) Reconstruction of the orthographic projectional geometry of the crystal in the lower right of Fig. 1, assuming that the $\{hhl\}$ facets are $\{229\}$. Here, the $\{100\}$ facet in the upper left of the projection is labelled as $(\bar{1}00)$, that near the centre of the projection is labelled as (001) and the one on the top right is labelled as (010) . The crystal has been taken to have external $m\bar{3}m$ symmetry with respect to the four $\{hhl\}$ facets surrounding $(\bar{1}00)$ and the eight $\{hhl\}$ facets bordering these four $\{hhl\}$ facets. To replicate what is seen with this crystal in Fig. 1, the eight $\{hhl\}$ crystal facets bordering the four $\{hhl\}$ facets surrounding the (100) facet have each been extended by the same amount along $[100]$. The projection direction with $\theta = 13^\circ$ and $\phi = 140^\circ$ is $[-0.172, 0.145, 0.974]$; the (100) facet is therefore not seen here. (b) As in (a), but showing the projection direction, drawn from the origin at the centre of the crystal to the black dot shown on the (001) surface very close to the edge common to the (001) and $(\bar{2}29)$ facets. (c) – (h) Reconstructions for the projection direction shown in (a) and (b) assuming that the $\{hhl\}$ facets are instead (c) $\{223\}$, (d) $\{112\}$, (e) $\{113\}$, (f) $\{114\}$, (g) $\{115\}$ and (h) $\{116\}$, respectively.

For the crystal in Fig. 2, the presence of the $(\bar{l}hh)$ facet evident in this image and its relative size seen in this image is useful in establishing that the predicted geometry for the $\{116\}$ form is inconsistent with the experimental evidence, because in Fig. 7(h) this facet is barely visible. By contrast, this $(\bar{l}hh)$ facet is all much too visible for the $\{113\}$, $\{112\}$ and $\{223\}$ forms. Once again, while both the predicted projections for

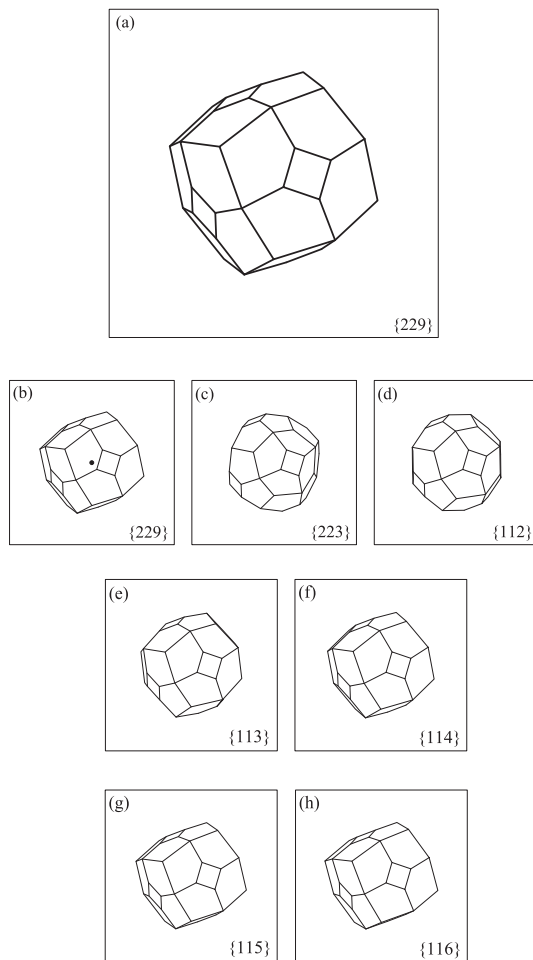


Fig. 7. (a) Reconstruction of the orthographic projectional geometry of the crystal in Fig. 2, assuming that the $\{hhl\}$ facets are $\{229\}$. The crystal has been taken to have external $m\bar{3}m$ symmetry in terms of its morphology. If the $\{100\}$ facet to the left of the projection is labelled as $(0\bar{1}0)$, that on the top is labelled as $(\bar{1}00)$ and that to the right of the centre of the crystal seen in this projection as (001) , then the projection direction with $\theta = 23^\circ$ and $\phi = 242^\circ$ is $[-0.183, -0.345, 0.921]$. (b) As in (a), but showing the projection direction, drawn from the origin at the centre of the crystal to the black dot shown on the $(\bar{2}29)$ facet. (c) – (h) Reconstructions for the projection direction shown in (a) and (b) assuming that the $\{hhl\}$ facets are instead (c) $\{223\}$, (d) $\{112\}$, (e) $\{113\}$, (f) $\{114\}$, (g) $\{115\}$ and (h) $\{116\}$, respectively.

the $\{114\}$ and $\{115\}$ forms fare well, that for $\{229\}$ strikes a sensible ‘best fit’ compromise.

Finally, for a comparison of the experimental predictions in Fig. 8 with the experimental image seen in Fig. 3, it is useful to look at the external perimeter of the crystal in Fig. 3 and see how faithfully this is reproduced in the predictions in Fig. 8. The ‘angularity’ of this perimeter is less faithfully reproduced for the $\{116\}$ form than for the $\{114\}$ and $\{115\}$ forms, all three of which are superior in their predictive abilities than the $\{113\}$, $\{112\}$ and $\{223\}$ forms. Once again, $\{229\}$ strikes a sensible ‘best fit’ compromise.

The predicted shapes of the crystals seen in projection were more sensitive to θ than to ϕ for the projections shown in these figures because of the choice made in labelling the $\{100\}$ facets seen in the scanning electron micrographs: changes in units of 0.5° for θ were found to be reasonable for the calculations, while changes in units of 1° were found to be reasonable for ϕ . A major conclusion from these calculations evident from Figs. 4–8 is that the deltoidal icositetrahedral $\{hhl\}$ facets

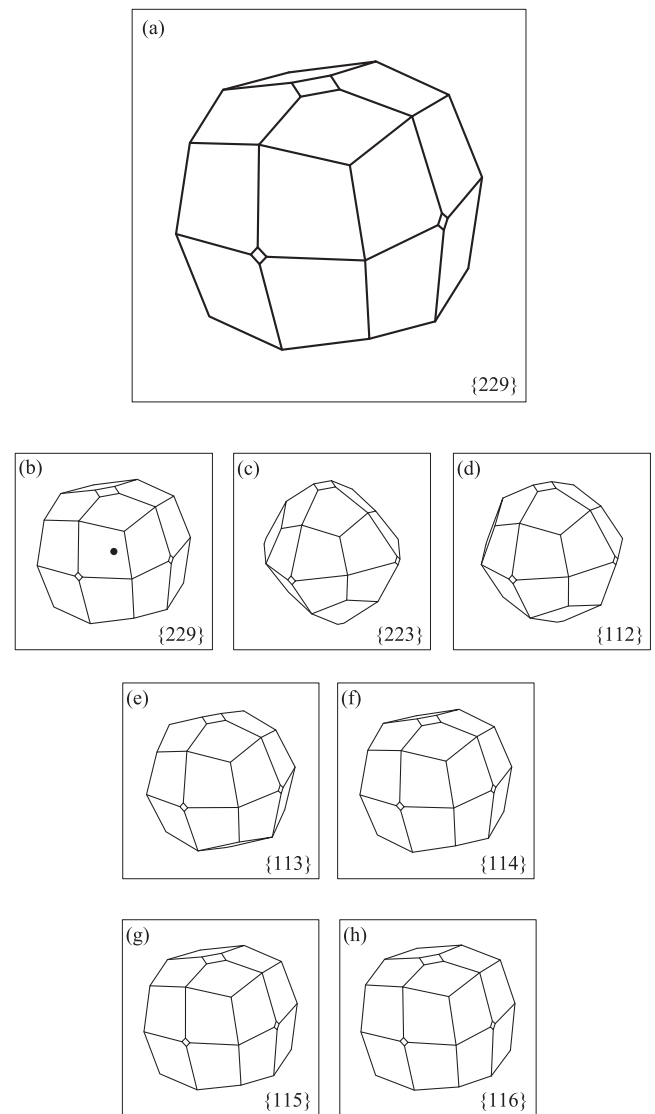


Fig. 8. (a) Reconstruction of the orthographic projectional geometry of the crystal in Fig. 3, assuming that the $\{hhl\}$ facets are all $\{229\}$. The crystal has been taken to have external $m\bar{3}m$ symmetry with respect to the $\{hhl\}$ facets. If the $\{100\}$ facet at the top of the projection is labelled as (010) , that on the lower left is labelled as (001) and that on the lower right is labelled as (100) . With $\theta = 40^\circ$ and $\phi = 36^\circ$, the projection direction is $[0.520, 0.378, 0.766]$. The (010) facet has been made larger than the (100) and (001) facets to be consistent with what is seen experimentally in Fig. 3. (b) As in (a), but showing the projection direction, drawn from the origin at the centre of the crystal to the black dot shown on the (229) facet. (c) – (h) Reconstructions for the projection direction shown in (a) and (b) assuming that the $\{hhl\}$ facets are instead (c) $\{223\}$, (d) $\{112\}$, (e) $\{113\}$, (f) $\{114\}$, (g) $\{115\}$ and (h) $\{116\}$, respectively.

were clearly not $\{112\}$, the minor facet geometry reported by Kovalenko et al. [8] in sub- μm sized $\alpha\text{-Fe}$ crystals annealed for 24 hr at 880°C .

4. Discussion

Recognition that the projectional geometry can be taken to be an orthographic projection for μm -sized single crystals observed in the scanning electron microscope, such as these b.c.c. Fe single crystals recovered from lunar samples, has enabled $\{229\}$ facets to be identified as a ‘best fit’ compromise on these Fe single crystals. These $\{229\}$ facets contrast with observations on iron crystals produced as single crystals on Earth, and also with observations of $\{110\}$ faceting on Fe crystals from the Haverö meteorite [11]. The predicted projection geometries for

{100} and {229} faceting in Figs. 4–8 of what are in practice truncated deltoidal icositetrahedra also help to interpret the contrast in the scanning electron microscope images of Figs. 1–3 produced from facets almost parallel to the electron beam, some of which has been lost in the printed versions of Figs. 2 and 3 in comparison with the original images. The predicted projectional geometry seen in Fig. 8 also confirms that the contrast and projectional geometry seen in Fig. 3, where two sets of {*hhl*} facets surround one of the $\langle 111 \rangle$ directions of this iron crystal, are together clearly rationalizable in terms of two sets of facets such as {114} and {115}.

Conditions for crystallization of these fine α -Fe single crystals have been established by Clanton et al. [1–4]. They quote an abundance of studies which indicate that a wide variety of minerals formed by vapour phase crystallization in the lunar environment [3,4]. Such crystallization conditions differ markedly from those used to produce α -Fe single crystals on Earth. Instead, they are merely indicative of the wide variety of conditions under which minerals are known to grow, such as ‘solutions often containing all manner of other substances as impurities’, as Phillips observes in Chapter I of his book [5]. It is highly likely that it is the local presence of such ‘impurities’ which has enabled these remarkable facets to grow on the five α -Fe crystals seen in Figs. 1–3 and to dominate their morphology. As others have noted in connection with growth from the vapour of various materials, a number of kinetic and thermodynamic processes are involved, as well as having favourable sites to enable atoms to be deposited, such as kink sites of atomic steps. The details of such growth is often system-specific and is also very temperature-dependent [14–17]. While outside the scope of this particular study, it would clearly be worthwhile scientifically to undertake such experiments to try and simulate the lunar environment within which these iron crystals will have been produced through vapour phase crystallization.

In practice, facets labelled {229} on a scale of a few hundred nanometres or more will themselves be structured at the atomic level, providing sites for continued growth. For example, ball models of tungsten (113) and tungsten (117) surfaces considered by Biernat and Blaszczyzyn [12] suggest that for these b.c.c. (117) surfaces, (001) terraces dominate the morphology at an atomic level and are linked by steps which have a common $[1\bar{1}0]$ vector with the (001) terraces to produce overall (117) surfaces, whereas for the (113) surfaces, there are (112) terrace ‘fragments’ and (001) steps. Faceting of atomically rough planar surfaces such as for iridium (210) surfaces at the scale of nanometres is known to be driven by chemical considerations caused by adsorbates [13]. Given such considerations, it is unsurprising that some of these lunar α -Fe single crystals have these exotic {229}-type morphologies. Clanton et al. found evidence of other α -Fe single crystal lunar morphologies which we have chosen not to analyse here, such as those shown in Figs. 9–11 of [2]. This is because of the dominance in these morphologies of the {100} cube form; this has the effect of making unambiguous analyses of the crystallography of the other forms more challenging because there is less information to be able to extract from these scanning electron microscopy images.

5. Conclusions

Crystallographic analysis of scanning electron microscopy images of small μm -sized single crystals of b.c.c. iron found on the surface of the Moon has shown that the deltoidal icositetrahedron faceting clearly seen is best described as {229} faceting. As others have noted [4], this faceting behaviour is indicative of the vapour phase crystallization in the lunar environment where the precise nature of the vapour and the temperatures of formation remain elusive. Recent studies of the way in which adsorbates enable surfaces to be fashioned at the nanometre level help to rationalise this unusual and rather photogenic faceting, but clearly it would be of interest to determine experimentally how this

faceting behaviour arose through vapour phase crystallization in the lunar environment.

Funding statement

This research did not receive any specific grant from funding agencies in the public, commercial, or not-for-profit sectors.

CRediT authorship contribution statement

Kevin M. Knowles: Conceptualization, Data curation, Formal analysis, Investigation, Methodology, Software, Validation, Visualization, Writing - original draft, Writing - review & editing. **Harshad K.D. H. Bhadeshia:** Formal analysis, Investigation, Writing - original draft, Writing - review & editing.

Declaration of Competing Interest

The authors declare that they have no known competing financial interests or personal relationships that could have appeared to influence the work reported in this paper.

Data availability

The authors are happy to share the Excel spreadsheets used for the analyses discussed in this manuscript.

References

- [1] U.S. Clanton, D.S. McKay, R.B. Laughon, G.H. Ladle, Crystal habit of iron in lunar breccias (extended conference abstract), Lunar Science-IV Volume 1 (1973) 143–145.
- [2] U.S. Clanton, D.S. McKay, R.B. Laughon, G.H. Ladle, Iron crystals in lunar breccias, Proceedings of the Fourth Lunar Science Conference, *Geochimica et Cosmochimica Acta* 1 (Supplement 4) (1973) 925–931.
- [3] U.S. Clanton, D.S. McKay, R.B. Laughon, G.H. Ladle, Trisioctahedral iron in lunar breccias (extended conference abstract), Lunar Science-V Volume 1 (1974) 126–128.
- [4] U.S. Clanton, D.S. McKay, R.B. Laughon, G.H. Ladle, Vapor-phase crystallization of iron in lunar breccias, Proceedings of the Fifth Lunar Conference, *Geochimica et Cosmochimica Acta* 1 (Supplement V) (1974) 621–626.
- [5] F.C. Phillips, *An Introduction to Crystallography*, 4th ed., Oliver & Boyd, Edinburgh, 1971.
- [6] B.E. Sundquist, A direct determination of the anisotropy of the surface free energy of solid gold, silver, copper, nickel, and alpha and gamma iron, *Acta Metall.* 12 (1964) 67–86.
- [7] L. Vitos, A.V. Ruban, H.L. Skriver, J. Kollár, The surface energy of metals, *Surface Science* 411 (1998) 186–202.
- [8] O. Kovalenko, F.O. Chikli, E. Rabkin, The equilibrium crystal shape of iron, *Scripta Mater.* 123 (2016) 109–112.
- [9] <https://moon.nasa.gov/resources/235/scanning-electron-microscope-view-of-iron-crystal/>, accessed 8 November 2022.
- [10] N. Cornille, Accurate 3D shape and displacement measurement using a scanning electron microscope, Ph.D. thesis, University of South Carolina, Columbia, U.S.A., and L’Institut National des Sciences Appliquées, Toulouse, France (2005), pp. 22–23.
- [11] J. Jedwab, Morphologies of iron crystals from the Haverö meteorite, *Meteoritics* 7 (1972) 537–546.
- [12] T. Biernat, R. Blaszczyzyn, Self-diffusion of tungsten on some facets of tungsten microcrystal, *Acta Physica Polonica A* 114 (Supplement) (2008) 11–16.
- [13] T.E. Madey, W.-H. Chen, H. Wang, P. Kaghazchi, T. Jacob, Nanoscale surface chemistry over faceted substrates: structure, reactivity and nanotemplates, *Chem. Soc. Rev.* 37 (2008) 2310–2327.
- [14] B.V. Spitsyn, L.L. Bouilov, B.J. Derjaguin, Vapor growth of diamond on diamond and other surfaces, *J. Crystal Growth* 52 (1981) 219–226.
- [15] E. Pearson, T. Takai, T. Halicioğlu, W.A. Tiller, Computer modelling of Si and SiC surfaces and surface processes relevant to crystal growth from the vapor, *J. Crystal Growth* 70 (1984) 33–40.
- [16] J.A. Venables, Atomic processes in crystal growth, *Surface Science* 299–300 (1994) 798–817.
- [17] Y. Homma, In situ observation of crystal growth by scanning electron microscopy, Chapter 23 of *Handbook of Crystal Growth, Fundamentals: Thermodynamics and Kinetics*, Volume I, Part A, Second Edition, ed. T. Nishinaga, Elsevier, Amsterdam (2015).